

# Evolution of Damage in All-Oxide Ceramic Matrix Composite After Cyclic Loading

Andreas Kupsch, René Laquai, Bernd R. Müller, Sidnei Paciornik, Jürgen Horvath, Kamen Tushtev, Kuroschi Rezwan, and Giovanni Bruno\*

While structural ceramics usually display a brittle mechanical behavior, their composites may show nonlinearities, mostly due to microcracking. Herein, the stiffness evolution of a sandwich-like laminate of an  $\text{Al}_2\text{O}_3$ –15%vol.  $\text{ZrO}_2$  matrix reinforced with Nextel 610 fibers is studied as a function of number of cycles  $N$  in tension. The stiffness of the composite degrades with increasing  $N$ , indicating microcracking. However, synchrotron X-ray refraction radiography shows that the internal specific surface of such cracks varies differently. A modeling strategy is developed for the calculation of the equivalent stiffness of mixtures (first the matrix and then the sandwich), based on the Voigt and Reuß schemes. The Bruno–Kachanov model is then used to estimate the initial microcrack density in the matrix (due to the thermal expansion mismatch) and the amount of microcracking increase upon cyclic loading. The stiffness in the composite degrades dramatically already after 20 000 cycles but then remains nearly constant. The combination of mechanical testing, quantitative imaging analysis, and modeling provides insights into the damage mechanisms acting: microcrack propagation is more active than microcrack initiation upon cyclic loading, but the second also occurs. This scenario is similar but not equal to previous results on porous and microcracked ceramics.

inherently brittle materials, a macroscopic pseudoductile behavior and nonbrittle failure of the composite could be achieved by “controlled” (micro) crack propagation in the matrix, where the fibers are protected against early failure.

Conditioned by the manufacturing process, the ceramic matrix is more susceptible to microcrack initiation when the composite is subjected to mechanical and/or thermal loads. The conventional concept to protect the fibers from high stress concentrations in the matrix is based on a weak interface.<sup>[2]</sup> Such weak interface allows debonding at the fiber–matrix boundary. In the case of so-called weak interface composites (WICs), the cracks propagating in the matrix are initially stopped or deflected into the fiber–matrix interface. The fibers remain initially intact, bridging the cracks and contributing to the higher load-bearing capacity of the composite. The initiation of the debonding process requires a low fracture energy of the interface,<sup>[3]</sup> which is usually realized

by coating the fibers with carbon or other highly anisotropic or porous ceramics.<sup>[4]</sup>


The weak interface in WIC allows the application of a high-quality ceramic matrix, which is comparable with the fibers in terms of stiffness. As a result, highest stiffness and strength of the composite are achieved. Moreover, the stress–strain

## 1. Introduction

The basic idea of a composite material made of a ceramic matrix reinforced by ceramic fibers is to enhance the damage tolerance and the reliability of conventional technical ceramics.<sup>[1]</sup> Although both components of such ceramic matrix composites (CMCs) are

A. Kupsch, R. Laquai, B. R. Müller, S. Paciornik, G. Bruno  
BAM  
Bundesanstalt für Materialforschung und -prüfung  
Unter den Eichen 87, 12205 Berlin, Germany  
E-mail: giovanni.bruno@bam.de

R. Laquai  
PTB  
Physikalisch-Technische Bundesanstalt  
Bundesallee 100, 38116 Braunschweig, Germany

 The ORCID identification number(s) for the author(s) of this article can be found under <https://doi.org/10.1002/adem.202100763>.

© 2021 The Authors. Advanced Engineering Materials published by Wiley-VCH GmbH. This is an open access article under the terms of the Creative Commons Attribution License, which permits use, distribution and reproduction in any medium, provided the original work is properly cited.

DOI: 10.1002/adem.202100763

S. Paciornik  
Department of Chemical and Materials Engineering  
PUC- Catholic University of Rio de Janeiro  
Rua Marquês de São Vicente 225, Gávea - Rio de Janeiro, RJ 22451-900, Brazil

J. Horvath, K. Tushtev, K. Rezwan  
Advanced Ceramics  
University of Bremen  
Am Biologischen Garten 2, Bremen 28359, Germany

K. Rezwan  
MAPEX - Center for Materials and Processes  
University of Bremen  
Am Biologischen Garten 2, Bremen 28359, Germany

G. Bruno  
Institute of Physics and Astronomy  
University of Potsdam  
Karl-Liebknecht-Str. 24-25, 14476 Potsdam, Germany

behavior of the composite is typically characterized by a well-pronounced elastic limit. The kink point in the stress–strain curve refers to the matrix fracture stress, above which the stiffness of the composite decreases. Load–unload cycles beyond the matrix fracture stress are used to determine the degradation of the composite stiffness as well as damage parameters, as defined in the classic damage mechanics,<sup>[5]</sup> that are widely used for modeling and prediction of the nonlinear behavior and the fracture of CMC.<sup>[6]</sup>

From a technological point of view, fiber coating is an expensive and time-consuming process. In contrast, the matrix is always the weaker part of the fiber-reinforced ceramic composites, as it has residual porosity and is therefore more prone to cracking. Based on the experience with porous interlayers as well as on considerations about crack formation and crack deflection mechanisms in porous ceramics, an alternative concept of ceramic fiber-reinforced composites with weak matrix (WMC) was successfully demonstrated in the 1990s.<sup>[7]</sup> The concept is based on a porous matrix with relatively high, but finely and homogeneously distributed, porosity, usually in the range of 30–40% vol. A strong fiber–matrix interface is tolerated as the fibers are protected from high stress concentrations by dissipating mechanical energy through irreversible large-area failure processes in the matrix.

In contrast to WIC, the elastic properties of WMC are strongly influenced by the properties of the fibers, the fiber orientation, and the fiber volume fraction, due to the significantly lower stiffness and strength of the porous matrix compared with the fibers. Depending on the fiber orientation, a strong anisotropy of the in-plane properties of the composite is expected. Especially when loaded in fiber direction, the mechanical performance of the fibers determines the composite properties, so that the WMCs usually show an apparently linear elastic behavior. Mechanical tests show almost no change in the stiffness of the composite until the ultimate failure. Nevertheless, based on acoustic emission (AE) analysis, it was found that in case of an almost macroscopically linear–elastic behavior, damage in the matrix occurs even at lower stresses.<sup>[8]</sup> As the mechanical properties of the matrix are decisive for the damage-tolerant behavior of the composite, it is of great importance to evaluate the damage in the composite after mechanical and/or thermal loading. When the damage in the composite cannot always be detected by direct evaluation of mechanical tests, additional methods such as AE are used in parallel. AE monitoring was successfully applied to analyze the damage evolution caused by both quasistatic and cyclic loads.<sup>[8b,9]</sup> However, the majority of the research studies related to the application of the AE technique for fatigue behavior are focused on the identification of the typical damage mechanisms in WIC. AE provides rather qualitative results, which could be helpful, for example, to determine the matrix fracture stress but is not suitable to reveal the anisotropy of the crack pattern. Most suited for this are 2D visualization by optical microscopy and 3D imaging techniques such as micro-computer tomography (XCT).<sup>[10]</sup>

The disadvantage of the two latter techniques is on the one hand that the preparation effort is very high (cutting and polishing) and on the other hand the very small sample size (e.g., 1 mm<sup>3</sup> for the highest spatial resolution ( $\approx 1 \mu\text{m}$  in XCT), which is not representative of a heterogeneous

material. X-ray refraction techniques,<sup>[11]</sup> on the other hand, combine high sensitivity for microcracks in the nanometer range with a large field of view (FOV) of several square millimeters.

X-ray refraction techniques were introduced a couple of decades ago<sup>[12]</sup> and have been successfully used for both materials characterization<sup>[11,13]</sup> and nondestructive testing.<sup>[14]</sup> Those techniques are used to obtain the amount of the relative internal specific surface of a specimen (i.e., surface per unit volume, relative to a reference state). They are, therefore, effective in the investigation of defects such as cracks and pores within ceramic components (see the study by Müller et al.<sup>[15]</sup>).

X-ray refraction occurs whenever X-rays interact with interfaces between materials of different densities as in the case of cracks, pores, and inclusions in a matrix. The difference of the refraction indices between the two interfacing materials, the so-called refraction decrement, determines the refraction angle at the interface. As the refraction decrement for X-rays is of the order of  $10^{-6}$ , X-ray optical effects can only be observed at very small angles of deflection, ranging from a few seconds to a few minutes of arc.<sup>[16]</sup> X-ray refraction techniques detect pores and cracks as soon as they exceed a size or opening of a few X-ray wavelengths. As the typical X-ray wavelengths are  $\approx 0.1 \text{ nm}$ , the smallest detectable object size is down to the nanometer range.<sup>[15a]</sup> This is not to be confused with the spatial resolution or the size of the individual objects that can be imaged. The spatial resolution of the technique is limited by the pixel size of the detector system. It must be emphasized that, because of the inevitable background noise, it is impossible to conclusively detect one single defect. A certain population of objects is necessary to yield an integrated signal above the background noise. X-ray refraction is primarily used in radiographic mode with thin specimens (platelets) and yields 2.5D information about the microstructure of the sample (i.e., integrated over the thickness but fully spatially resolved in the other two directions). This analysis can be made on samples of macroscopic size (say, a few cm), that is, the field-of-view (FOV) of X-ray refraction techniques is much larger than that of high-resolution XCT and of classic microscopy. Furthermore, X-ray refraction techniques are sensitive to defect orientation, thereby allowing different kinds of defects to be identified (e.g., flat cracks vs. round pores). The refraction signal of an isotropic inhomogeneity, such as spherical voids, is present at any orientation of the specimen, whereas for cracks or elongated pores, the signal decreases when the defect surface normal is perpendicular to the scattering plane of the experiment.

In this work, we will see how the X-ray refraction signal can be quantitatively correlated with damage evolution and support micromechanical models (as done in other studies<sup>[11,15,17]</sup>) to understand the mechanical behavior of CMCs.

## 2. Experimental Section

### 2.1. Materials

The material used in this work was the commercial composite Keramikblech-type FW12, provided by the company Walter E. C. Pritzkow Spezialkeramik, Germany.<sup>[18]</sup> The composite

consisted of 12 layers of Nextel 610 0/90° fiber fabrics DF11-1500-8HS (3M Company, St. Paul, MN, USA) and was produced by slurry infiltration and pressing. The matrix composition was 85 wt% of alumina and 15 wt% of zirconia stabilized with 3 mol% of yttria. Dog-bone specimens with total length of 150 mm and a reduced section of 40 mm × 10 mm were water jet cut out from a 2.9 mm-thick composite sheet. To characterize the mechanical properties of the material, tensile specimens with 0/90° and with ±45° fiber orientation relative to the load axis were cut out from the batch. For the cyclic tests, one single specimen with 0/90° fiber orientation relative to the tensile axis was used, which underwent all mechanical testing and imaging experiments.

## 2.2. Characterization Methods

The composite microstructure was observed with a scanning electron microscope (SEM) model Zeiss Series EVO (Carl Zeiss Microscopy Ltd., Cambridge, UK). For the SEM analysis, samples were embedded in epoxy resin and ground and polished for surface finish. SEM images in secondary electron (SE) mode were taken with an electron current of 10 pA, a sample detector distance of 10.3 mm, and a voltage of 15 kV. Porosity (nearly all open) and pore size distribution were measured via mercury intrusion using a porosimeter Pascal 140/440 (Microtrac Retsch GmbH, Haan, Germany). A sample with dimensions ≈ 3 × 8 × 10 mm<sup>3</sup> was tested. The mechanical properties of the composite in the fiber directions mentioned earlier were evaluated with quasistatic tensile tests according to DIN EN 658-1. The tests were conducted with a universal testing machine Kappa 050 DS (Zwick Roell Group, Ulm, Germany), equipped with a laser extensometer PS-E50-0138-AM (Fiedler Optoelektronik GmbH, Lutzen, Germany) for strain measurement. Three tensile samples were tested with a crosshead speed of 1 mm min<sup>-1</sup>.

The fatigue tests were conducted with a servo-hydraulic testing machine Roell Amsler (Zwick Roell Group, Ulm, Germany), equipped with an MTS control system (MTS Systems GmbH, Germany). The specimen was loaded cyclically with a sinusoidal force vs. time function. The test frequency was 100 Hz and the

ratio of the minimum stress ( $\sigma_{\min}$ ) to the maximum stress ( $\sigma_{\max}$ ) was  $R = 0.1$ . The peak values of the load  $F_{\max}$  and  $F_{\min}$  were recorded for all cycles. A laser extensometer PS-E50-0138-AM (Fiedler Optoelektronik GmbH, Lutzen, Germany) was used for strain measurement. The gauge length was 25 mm.

Before and after each cycle, two additional triangular cycles were conducted at a low crosshead speed (200 N s<sup>-1</sup>) to determine Young's modulus (Figure 1).

The cyclic loading of the sample was conducted in four blocks, each of which with a different maximum stress and duration, but all with the same stress ratio  $R = 0.1$ . The first loading block of 10 000 cycles had a maximum stress equal to 3/5 of the tensile strength ( $\sigma_B$ , determined in a quasistatic test on three samples). The second loading block was again 10 000 cycles but with a higher load (4/5  $\sigma_B$ ). The third and fourth loading blocks were conducted at the same load level of 4/5  $\sigma_B$  but each with 500 000 cycles. In total, the sample was loaded for 1 020 000 cycles.

It is to be remarked that our goal was not to determine fatigue properties, but to follow the damage evolution due to cyclic loading. Therefore, we concentrated on the analysis of one single sample: we will also show that the reproducibility of the mechanical properties confirmed the robustness of this strategy.

## 2.3. X-Ray Refraction

Synchrotron X-ray refraction radiography (SXRR) measurements were carried out at the BAM synchrotron laboratory BAMline at Helmholtz-Zentrum Berlin, Germany.<sup>[19]</sup> One single specimen was measured in the as-produced state and after each loading block, a total of five times. This avoided comparing sister samples and ensured the best reproducibility, as well image registration. The time plan of cyclic loading and X-ray characterization is shown in Figure 2.

A highly collimated monochromatic X-ray beam was used for SXRR experiments (relative energy band width of 0.2%). The beam energy was set to 30 keV to achieve a specimen X-ray transmission of about 10%. A highly dynamic charge-coupled device (CCD) camera (pco.1600, 1600 × 1200 pixel, 14 bit,

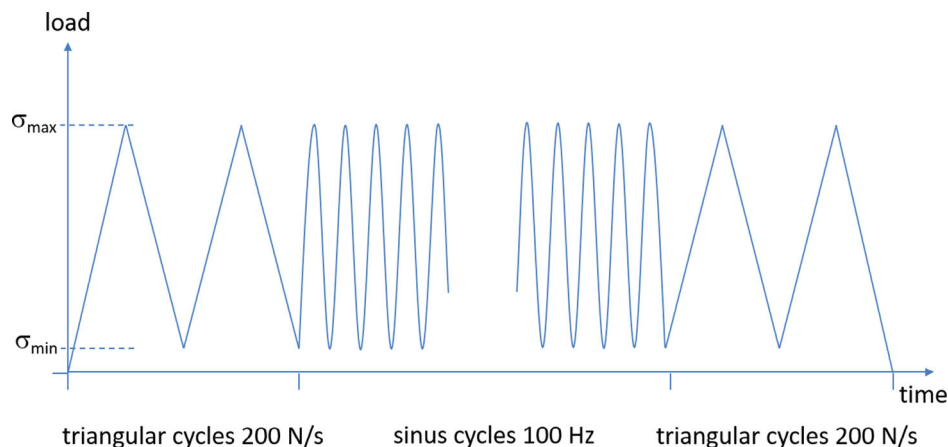


**Figure 1.** Schematic representation of the cyclical tests conducted in one loading block.

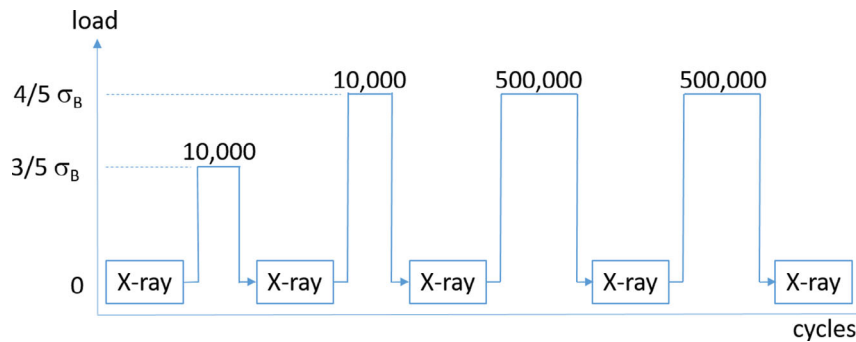


**Figure 2.** Graphical overview of the conducted cyclic loading and the X-ray characterization.

thermoelectric cooled, PCO AG, Kelheim, Germany) in combination with a lens system and a 50  $\mu\text{m}$ -thick cadmium tungstate (CWO) scintillator screen provided a pixel size of 4.08  $\mu\text{m} \times 4.08 \mu\text{m}$ , capturing a FOV of about 6.3 mm  $\times$  4.7 mm. The incident beam was narrowed to the FOV by a slit system to avoid detector backlighting.<sup>[20]</sup> The exposure time for each image was 2 s. The same specimen cyclically loaded at the University of Bremen was measured in five different sessions, see Figure 2. To intercalibrate the measurements, an unloaded reference (sister) specimen was also measured each time together with the loaded specimen.

A Si (111) analyzer crystal was placed in the beam path between the specimen and the camera system, as shown in **Figure 3**, to conduct refraction radiographs. The crystal was aligned in the X-ray beam in such a manner that the Bragg condition was fulfilled (Bragg angle  $\theta_B = 3.779^\circ$  at 30 keV, angle between the incident beam direction and the crystal surface) and the free X-ray beam (without sample) was completely reflected into the detector.

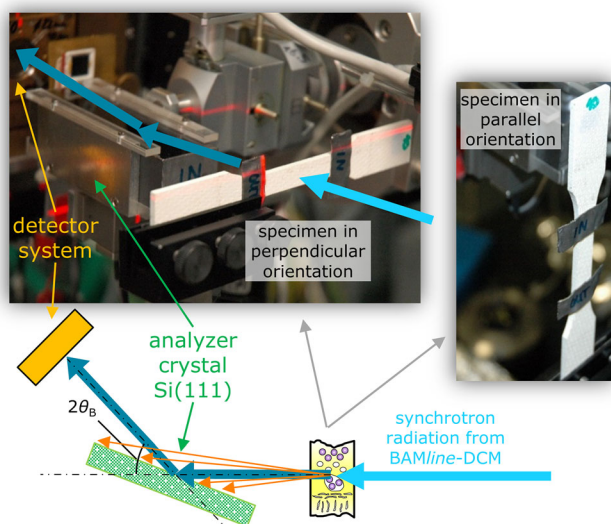


**Figure 3.** Sketch and photograph of the measurement setup of the X-ray refraction station at BAMline. The light blue arrow indicates the incident beam, the dark blue arrow indicates the attenuated beam, and the orange arrows indicate the refracted rays.

beam, only the rays that still fulfilled the Bragg condition would be reflected to the detector, all other rays (that would be deflected at internal interfaces such as pores or cracks) would not be detected. Thus, the intensity measured in all detector pixels was not only reduced by the (local) absorption of the specimen, but also by refraction phenomena. To determine the sole local specimen absorption properties, the specimen was measured in standard transmission mode, that is, without the analyzer crystal in the beam. For the refraction radiography measurements, the specimens were measured in two orientations, in the following named “perpendicular” (the longitudinal axis of the specimen and the load direction were perpendicular to the scattering plane) and “parallel” (the longitudinal axis of the specimen and the load direction were parallel to the scattering vector -the bisectrix of the angle identified by the incident and refracted beam-, see Figure 3). In addition, dark-field (beam-off) and flat-field (beam-on, without specimens) images were acquired to correct all images. To cover as large a specimen area as possible, SXRR and transmission images were taken at several adjacent specimen areas. The images were stitched afterward, so that a specimen area of about 24 mm  $\times$  5 mm was available for analysis. Using the image analysis software “Fiji Image J”<sup>[21]</sup> the attenuation ( $\mu \cdot t$ ) and the refraction value ( $C_m \cdot t$ ) were evaluated for each pixel according to Equation (1) and (2), respectively, with  $C_m$  being the refraction value,  $\mu$  being the attenuation coefficient, and  $t$  the (local) sample thickness. For a detailed description of data processing and evaluation, the reader is referred to the study by Nellesen.<sup>[22]</sup>

$$\mu \cdot t = -\ln\left(\frac{I}{I_0}\right) \quad (1)$$

$$C_m \cdot t = 1 - \frac{I_R}{I_{R0}} \cdot \frac{I_0}{I} \quad (2)$$

In Equations (1) and (2)  $I$  and  $I_0$  are the transmission intensity with and without sample, respectively, and  $I_R$  and  $I_{R0}$  are the refraction intensity with and without sample, respectively. The influence of the specimen thickness  $t$  was eliminated by dividing the local refraction value ( $C_m \cdot t$ ) by the local absorption property ( $\mu \cdot t$ ). This yielded the relative specific refraction value ( $C_m/\mu$ ), which is correlated with the relative specific (internal) surface of the specimen. Note that absolute values can be determined if an instrument calibration is conducted with a calibration sample

with known specific surface and identical absorption properties. In our case, this calibration was not necessary, as the *evolution* of damage was investigated.

### 3. Results

#### 3.1. Material Characterization

Figure 4 shows some SEM pictures of the composite. The picture with lower magnification (Figure 4a) reveals relatively large matrix-rich regions between the fiber layers as well as some large voids. The last ones probably originated by entrapped air during the stacking step of composite processing. Macroscopic cracks, which could occur during drying and sintering steps, are not observed. Figure 4b shows fibers that are embedded and completely enclosed by the porous matrix. It can be concluded that a good degree of infiltration of the fiber fabrics was obtained. No fiber debonding seems to be present in the as-produced conditions.

The total porosity of the composite, determined by mercury intrusion, was 27.9%. The mercury intrusion curve (Figure 5) shows a bimodal pore size distribution with maxima at about 0.1  $\mu\text{m}$  and 2  $\mu\text{m}$ . The first maximum is very well pronounced and is in accordance with the matrix fine porosity. The maximum at about 2  $\mu\text{m}$  can be associated with voids within the fiber bundles (see Figure 4a).

As shown in Figure 4a, there are also significantly larger pores (>120  $\mu\text{m}$ ), which could not be detected by our mercury intrusion device. Further characteristics of the composite material are shown in Table 1.

Due to the high porosity and the absence of fiber coating, the composite under investigation can be classified as a WMC. The expected strong anisotropy of the mechanical properties was experimentally confirmed, as shown in Table 1, where the elastic modulus and the tensile strength in two material directions are given. Under uniaxial on-axis quasistatic tensile load ( $0^\circ$ , fibers are oriented in load direction), the oxide fibers provide high stiffness and strength of the composite. In contrast, the strength and

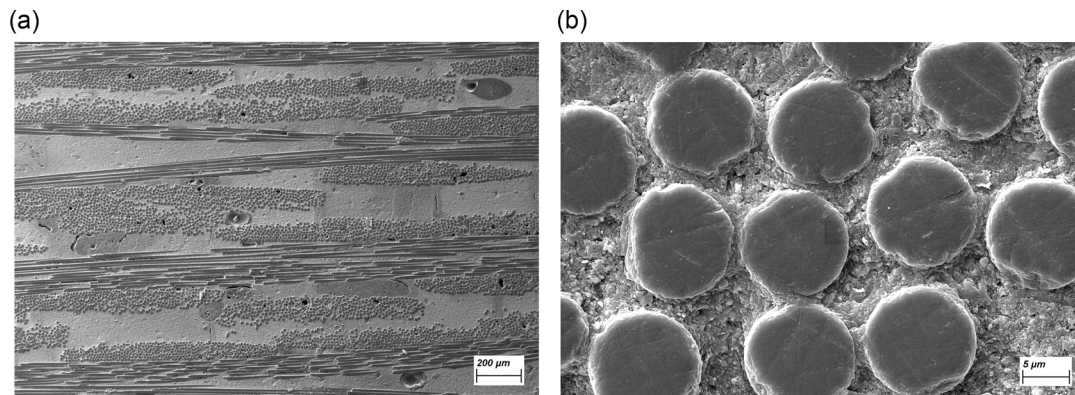


Figure 4. Microstructure of the tested composite FW12 at two different magnifications.

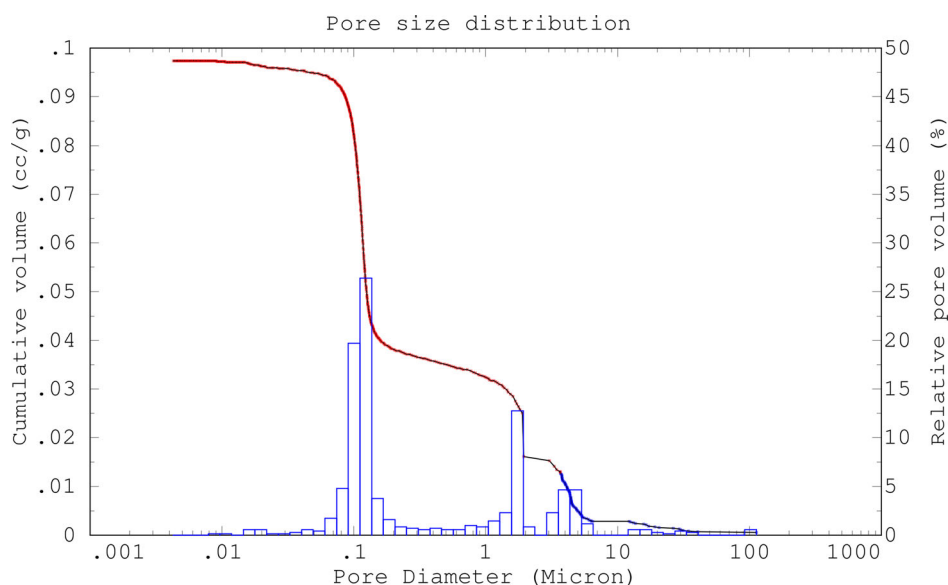


Figure 5. Mercury intrusion curve (continuous curve) and equivalent pore size distribution (histogram).

**Table 1.** Physical and mechanical properties of composite FW12.

Fabric type	Load direction	No. of layers	Average Thickness, $t$ [mm]	Fiber Content, $c_{\text{fiber}}$ [vol%]	Total porosity $\rho_{\text{total}}$ [%]	Young's modulus $E$ [GPa]	Tensile strength [MPa]
DF11 – 1500-8HS	0°	12	2.9	39.6	27.9	97 ± 1	257 ± 11
	45°					64 ± 2	89 ± 2

the stiffness are strongly reduced under off-axis conditions, in this case 45°, because the fibers are not efficiently carrying the load.

Significant shape differences of the stress–strain curves in the on-axis and the off-axis quasistatic tensile tests are also observed

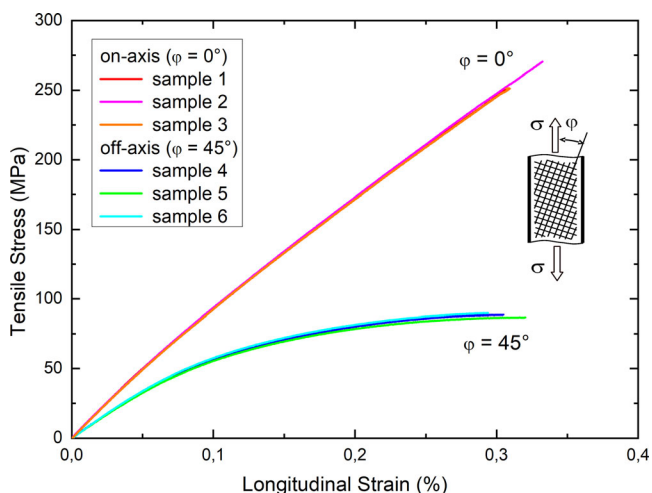


**Figure 6.** Quasistatic tensile stress versus strain curves of six samples of composite FW12, three loaded in on-axis (0°, loading in the direction of the fibers) and three off-axis (loading in 45° to the fiber orientation) directions.

(Figure 6). In the 0° direction, the composite behaves almost linear–elastic up to ultimate failure, although the slope of the curves slightly decreases starting at ≈25 MPa. In the 45° direction, damage already occurs at low stresses. The stiffness of the composite decreases continuously until the material fails at relatively low stress. Figure 6 shows a very good reproducibility of the tensile properties in all investigated directions; it also indicates a consistent microstructure among different specimens of the composite.

### 3.2. Fatigue Test Examination

As described in Section 2.2, the fatigue tests were conducted at two different stress levels corresponding to 3/5 and 4/5 of the quasistatic tensile strength. Both maximum stress levels significantly exceeded the stress at which the first nonlinearities appear in the quasistatic stress–strain curves in 0° direction. Therefore, it was expected that the composite would also be damaged under cyclic loading, although it was not a priori known whether cracks would appear only in the matrix, or the fibers would also fail. Unloading and reloading cycles on the composite in the as-received condition and after each loading block (see Figure 2) are shown with an offset of 0.2% strain for better visualization in Figure 7. First of all, it should be mentioned that the load and unload curves are superimposed and no hysteresis is observed in any of the cycles. The young's modulus decreases with increasing

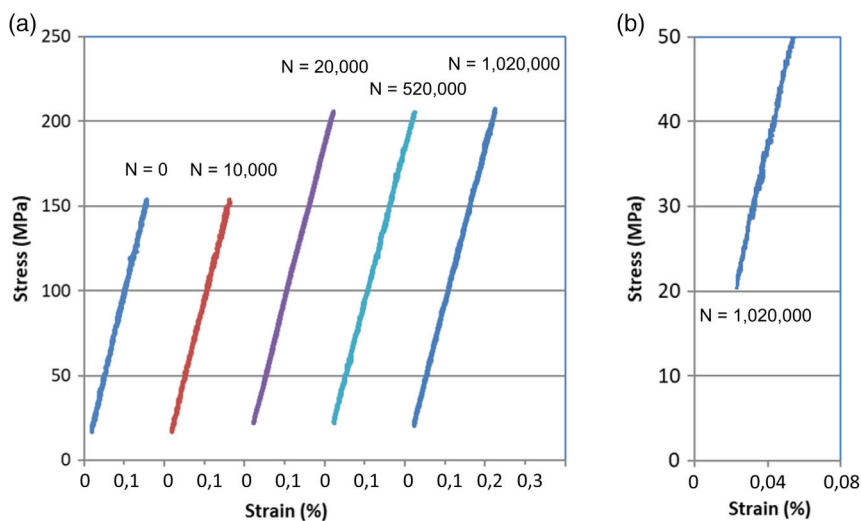


**Figure 7.** a) Quasi-static load/unload stress–strain curves after each cyclic loading block (see Figure 2). The value  $N$  indicates the number of cycles completed before the loading and unloading curves are recorded. As the slope does not differ much after different number of cycles, the curves are shown with offset of 0.2% strain. b) Zoom of the load/unload stress–strain curves after 1 020 000 cycles up to 50 MPa. No hysteresis can be discerned: the load and unload branches overlap.

number of cycles (see Table 2). This indicates that damage does occur during the cyclic tests.

### 3.3. X-Ray Refraction

Figure 8-top exemplarily shows the local absorption properties, ( $\mu \cdot t$ ) map, as a 2D grayscale image (the gray value range is indicated in the inset top right) of the loaded specimen after 520 000 load cycles (of 4/5 of the maximal load). Different gray levels indicate inhomogeneities in the density distribution, captured with the spatial resolution of the image (about  $4 \mu\text{m} \times 4 \mu\text{m}$ ). The mean absorption coefficient, averaged over the image, in parallel and perpendicular orientation of the specimen with respect to the scattering vector is shown in Figure 8-bottom, as a function of load cycles. No quantitative differences between the two orientations and as a function of the number of cycles can be found. This implies that the material did not undergo any microstructural change (affecting its X-ray absorption).

In contrast, the relative specific surface does evolve in the course of cyclic loads. As mentioned in the Sections 1 and 2.3, X-ray refraction techniques are sensitive to defect

orientation and can be used to classify such defects.<sup>[23]</sup> Figure 9 shows the orientation-dependent spatial distribution of the relative specific surface values ( $C_m/\mu$ ) for three different load states (unloaded state, after 520 000, and after 1 020 000 load cycles) as 2D grayscale images (maps). The same sample section is shown in all six images. In the images labeled as “parallel,” the longitudinal axis of the specimen was oriented parallel to the scattering vector (the bisectrix of the angle identified by the incident and refracted beam). In this position, one can detect internal surfaces (e.g., cracks) that are oriented perpendicular to the load direction. In the images labeled as “perpendicular,” the specimen axis was oriented perpendicular to the scattering vector. In this position, internal surfaces oriented parallel to the load direction are detected. The mean values for each state and both sample orientations are shown in the bar graph in Figure 10. The values after 10 000 and 20 000 load cycles do not differ from the values of the initial (virgin) state, within the measurement uncertainty. The spatial distribution (captured with a spatial resolution corresponding to a pixel size of about  $4 \mu\text{m} \times 4 \mu\text{m}$ ) of gray levels seems also to be similar, that is, no significant local change is observed. This means that no additional internal surfaces are created before 20 000 cycles. Only after 520 000 cycles the value of the relative specific surface increases by  $\approx 15\%$  for the parallel specimen orientation. Interestingly, the value for the perpendicular orientation remains unchanged. As  $C_m/\mu$  is proportional to the amount of inner surfaces (discontinuities, pores, cracks), it can be stated that cracks or fiber–matrix debonding evolve during the cyclic loading process, and these interfaces are oriented perpendicular to the load direction. After 1 020 000

**Table 2.** Composite elastic modulus after different number of loading cycles extracted from a linear fit of both load and unload branches of the curves shown in Figure 7a.

Number of cycles	0	10 000	20 000	520 000	1 020 000
Elastic modulus (GPa)	99.5	93.5	91.4	91.0	90.9

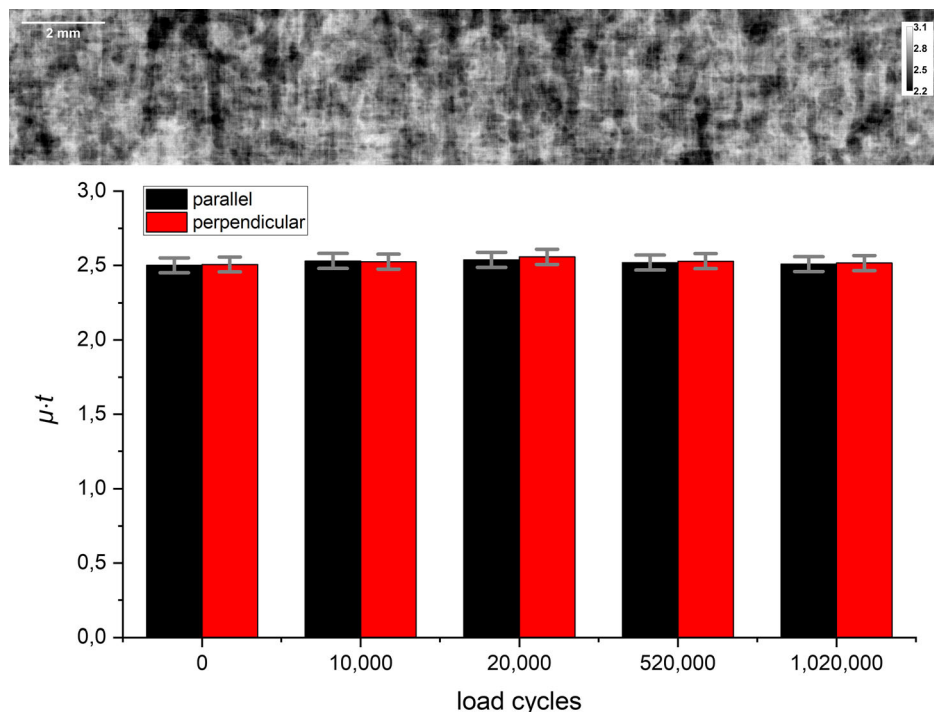


**Figure 8.** Top. ( $\mu \cdot t$ ) Map as 2D grayscale images of the loaded specimen after 520 000 load cycles (of 4/5 of the maximum load). High ( $\mu \cdot t$ ) values are shown as bright, low values as dark. Bottom. ( $\mu \cdot t$ ) Mean values of the 2D images for the test sample in the unloaded state and after four load levels for two orientations with respect to the scattering vector. The error bars indicate the standard deviation of local values measured for ( $\mu \cdot t$ ) across the specimen, that is, the level of inhomogeneity of the spatial distribution of defect.

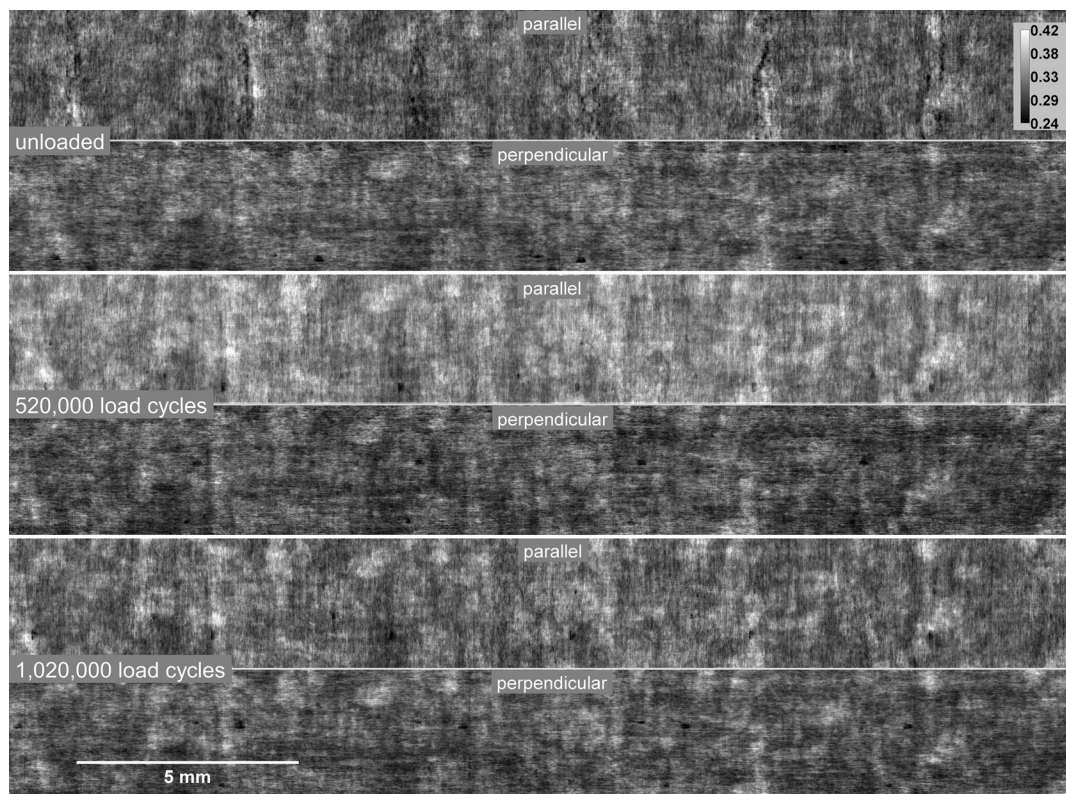


**Figure 9.** Maps of the relative specific surface  $C_m/\mu$  of the test specimen in: the initial state (top), after 520 000 (middle), and after 1 020 000 (bottom) load cycles at 4/5 of the maximum load). Bright gray values indicate areas of high, dark values of low specific surface values. The gray scale is the same for all images (indicated in the inset top right).

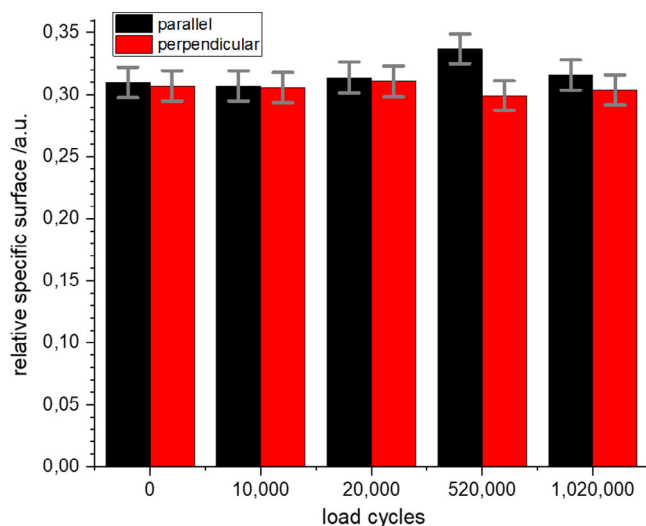


**Figure 10.** The mean value of the relative specific surface of the test sample for both orientations in the unloaded state and after four load cycle steps.

load cycles the  $C_m/\mu$  values decrease and return to the level of the unloaded specimen. This feature will be discussed in the next section.

We finally remark that, thanks of its large FoV, SXRR contains microstructural information equivalent to several tens or even

hundreds of SEM pictures, that is, statistically representative of the material. The inhomogeneity of the microstructure is given in the form of an error bar in Figure 10. This number can also be interpreted as the variability among different specimens.

#### 4. Discussion

**Figure 11** (left) shows the frequency distributions of the  $C_m/\mu$  values of Figure 9 for three different load states (unloaded state, after 520 000, and after 1 020 000 loading cycles) for the two orientations of the specimens. The center position and the full width of half maximum (FWHM) of the log-normal fitting function are shown in **Table 3** and visualized as an inset in Figure 11 (right). The FWHM is an indirect measure of the specific surface. In fact, let  $A$  be the integral intensity of the rocking curve; then,  $A \sim I_R \times \text{FWHM}$ , that is, the effect of refraction is an angular redistribution of the intensity, whereas the integral remains constant. The FWHM continuously increases with increasing number of cycles. Except for the condition at 520 000 load cycles, the values for the parallel and perpendicular specimen orientation are almost identical. The center position of the distributions shows different trends: for the parallel orientation, it first increases and then decreases, whereas for the perpendicular orientation, it slightly decreases (and then increases back the original values). The sample after 520 000 load cycles has the highest



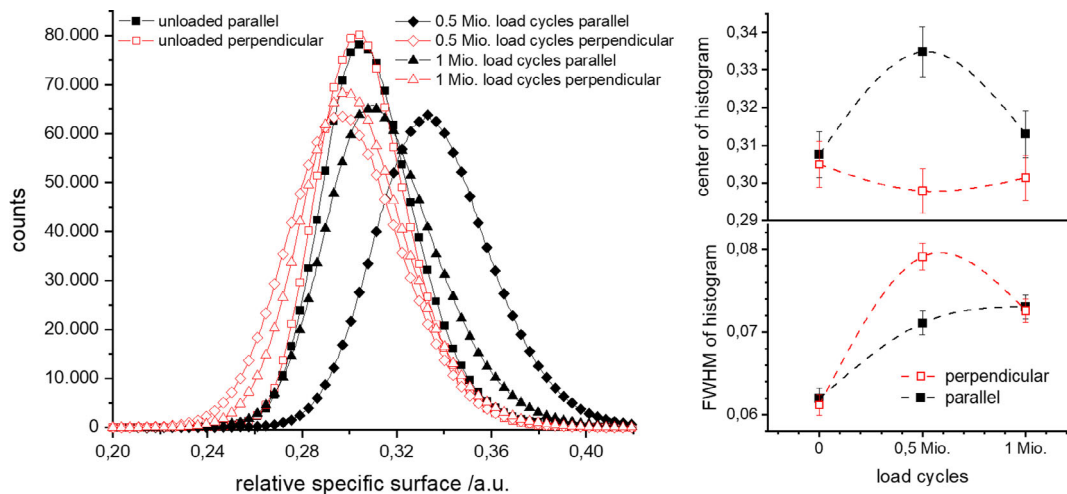


**Figure 11.** Frequency distributions of the relative specific surface values (left) of three different load states (unloaded state, after 520 000, and after 1 020 000 loading cycles): a comparison between parallel (black solid symbols) and perpendicular (red open symbols) specimen orientation. The center position and FWHM of the distributions are visualized in the graphs on the right.

**Table 3.** Fitted parameters of the XRRR rocking curves.

Load cycles	Orientation	Center of distribution	FWHM
0	Perpendicular	$0.305 \pm 0.006$	$0.061 \pm 0.002$
	Parallel	$0.308 \pm 0.006$	$0.062 \pm 0.002$
0.5 Mio.	Perpendicular	$0.298 \pm 0.006$	$0.079 \pm 0.002$
	Parallel	$0.335 \pm 0.006$	$0.071 \pm 0.002$
1 Mio.	Perpendicular	$0.301 \pm 0.006$	$0.073 \pm 0.002$
	Parallel	$0.313 \pm 0.006$	$0.073 \pm 0.002$

value of the distribution center position in its parallel orientation, but after additional 500 000 load cycles (1 020 000 in total), we observe a decrease of  $C_m/\mu$  to values similar to those of the unloaded sample. An analogous behavior was observed in  $\beta$ -eucryptite ceramics:<sup>[15a]</sup> in such work, it could be calculated that the total internal microcrack surface would decrease after loading, due to microcrack coalescence favoring the closure of smaller microcracks.

The explanation for the contemporary decrease in stiffness and relative specific surface (observed in the study by Müller et al.<sup>[15a]</sup>) was microcrack shielding of a large amount of small cracks, induced by propagation of large cracks. This was confirmed by Monte Carlo calculations.

In the present case, the scenario is similar but not identical. 1) We first have microcrack propagation (well below 520 000 cycles): the internal specific surface stays constant while the stiffness decreases (and the microcrack density increases). 2) We then have both nucleation and propagation of microcracks (see below) and therefore the internal specific surface increases; at this point the stiffness and the microcrack density stay nearly constant, and the newly nucleated microcracks have a negligible density (i.e., their radii are small). 3) Finally, the crack shielding effect takes over (the relative internal specific surface decreases

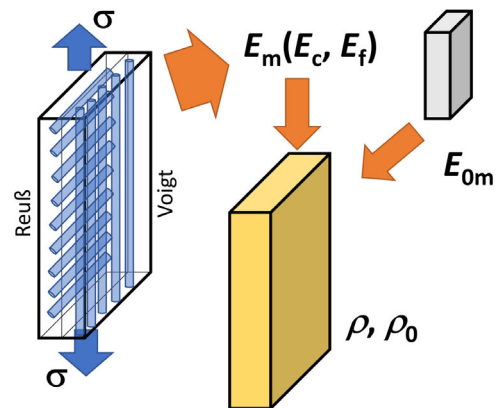


**Figure 12.** Sketch of the modeling strategy to calculate the equivalent matrix stiffness and the microcrack density parameter ( $E_m$ ,  $E_{0m}$ ,  $E_f$ ,  $E_c$  = matrix, dense matrix, fiber, and composite stiffnesses). See the text for details.

and small microcracks close, as they are not any longer under load) while the stiffness remains constant.

Indeed, as mentioned in the study by Müller et al.,<sup>[15a]</sup> the fact that the specific surface decreases due to microcrack closure does not imply that damage decreases, because damage depends on the microcrack density parameter  $\rho = \frac{1}{V} \sum_i a_i^3$ , which is heavily impacted by the largest microcracks, not by the smallest ones ( $a_i$  = radius of the  $i$ -th [penny-shaped] microcrack,  $V$  the observation volume, and the sum runs over all the microcracks contained in  $V$ ; see the study by Bruno et al.<sup>[24]</sup>).

To calculate the amount of microcracking before, during, and after the loading cycle, we adopted the following modeling strategy (see Figure 12):. 1) We first modeled the specimens as an alumina/zirconia matrix composite with two layers, one with fiber orientation  $0^\circ$  and the other with orientation  $90^\circ$ , and calculated the equivalent Young's modulus (note that fabrics are

reasonably approximated as parallel fibers). 2) We assumed that porosity is concentrated in the  $\text{Al}_2\text{O}_3 + 15\%\text{ZrO}_2$  matrix; as we know the Young's modulus of the fibers (total volume fraction: 40%) and we measured that of the composite, we calculated the equivalent Young's modulus of the matrix; This is the stiffness of the matrix containing porosity and microcracking; 3) We used the Hill's average<sup>[25]</sup> between the Reuß<sup>[26]</sup> and the Voigt<sup>[27]</sup> models to estimate the stiffness of the undamaged and dense matrix (85%vol  $\text{Al}_2\text{O}_3$  and 15%vol  $\text{ZrO}_2$ ). 4) We took the Bruno and Kachanov approach<sup>[24b,28]</sup> to estimate the microcrack density parameter, assuming spherical pores (such assumption is justified by the fact that matrix pores have nanometer size).

The laminate consists of two layers, with fibers oriented at 90° to one another (Figure 12); this means that the equivalent stiffness of such layers can be calculated using the Reuß average,  $E_R$ , for the part containing fibers perpendicular to the load direction, and with the Voigt average,  $E_V$ , for that containing fibers parallel to the load direction.

According to the two schemes

$$\begin{cases} E_R = \nu_m E_m + \nu_f E_f \\ \frac{1}{E_V} = \frac{\nu_m}{E_m} + \frac{\nu_f}{E_f} \end{cases} \quad (3)$$

where  $\nu_m = 0.6$  and  $\nu_f = 0.4$  are the matrix and fiber volume fractions, respectively, and  $E_m$  and  $E_f$  are the respective stiffnesses ( $E_f = 370$  GPa is known from the 3M datasheets<sup>[29]</sup> and  $E_m$  is at this point still unknown). To combine the two layers, we again use Voigt average (two parallel plates containing the load axis); as the two have the same volume fraction (0.5), the composite stiffness will then be

$$\frac{1}{E_C} = \frac{1}{2E_R} + \frac{1}{2E_V} \quad (4)$$

If we insert Equation (3) in (4) we get a second-degree algebraic equation in  $E_m$  with coefficients function of the volume fractions of matrix and fibers ( $\nu_m$  and  $\nu_f$ ) as well as stiffness of the fibers (from literature) and of the composite (measured), all known quantities. The solution reads

$$E_m = \frac{E_f}{2\nu_m} \left\{ \left[ \frac{(1 + \nu_m^2)E_C}{2E_f - \nu_f E_C} - \nu_f \right] \pm \sqrt{\left[ \frac{(1 + \nu_m^2)E_C}{2E_f - \nu_f E_C} - \nu_f \right]^2 + \frac{4\nu_f \nu_m^2 E_C}{2E_f - \nu_f E_C}} \right\} \quad (5)$$

One of the roots of the equation is negative and must be discarded. In the final formula only the positive sign must be taken into consideration.

The same idea can be used to estimate the stiffness of the microcrack-free and dense matrix,  $E_{0m}$ , starting from the stiffnesses of the constituents ( $E_A = 360$  GPa for the alumina, assumed to be that of Kyocera A479 white alumina and  $E_Z = 200$  GPa for the zirconia, assumed to be Kyocera Z201N ivory); we use in this case Hill's ansatz, that is, the average of the Reuß and the Voigt averages.

$$\begin{cases} E_{Rm} = \nu_A E_A + \nu_Z E_Z \\ \frac{1}{E_{Vm}} = \frac{\nu_A}{E_A} + \frac{\nu_Z}{E_Z} \end{cases} \quad (6)$$

We take the average

$$E_{0m} = \frac{1}{2} \cdot (E_{Rm} + E_{Vm}) = \frac{1}{2} \frac{\nu_A \nu_Z (E_A^2 + E_Z^2) + (1 + \nu_A^2 + \nu_Z^2) E_A E_Z}{\nu_A E_Z + \nu_Z E_A} \quad (7)$$

and obtain  $E_{0m} = 329$  GPa. This is the (theoretical) Young's modulus of the matrix with neither porosity nor microcracking.

Finally, following the treatment proposed in the study by Bruno et al.,<sup>[24]</sup> the dependence of the tangent modulus of the matrix mixture ( $E_m$ , containing both microcracks and porosity) at the origin of the stress-strain curve (i.e., the Young's modulus or stiffness in our case) can be described by the equation

$$\frac{E_m}{E_{0m}} = (1 - p)^n \cdot \exp(-C_2 \rho) \quad (8)$$

Equation (8) takes into account the influence of porosity  $p$ . In our case we have to take the matrix porosity, as the fibers are assumed to have no pores. The matrix porosity  $p$  is simply calculated from  $p = p_{\text{total}} / (1 - c_{\text{fiber}}) = 0.46$  (values for  $p_{\text{total}}$  and  $c_{\text{fiber}}$  from Table 1). Moreover, Equation (8) takes into consideration the microcrack density parameter, which contributes to the decrease in stiffness from the undamaged material;  $n$  is the so-called pore shape factor (see other studies<sup>[30,31]</sup>), which is equal 2 for spheres, and  $C_2 = \frac{16 \cdot (1 - \nu_0^2) \cdot (10 - 3\nu_0)}{45 \cdot (2 - \nu_0)}$  is a constant depending on Poisson's ratio  $\nu_0$  of the dense material (we take  $\nu_0 = 0.23$  for the dense matrix; hence,  $C_2 = 1.77$ ). In fact, using Equation (8) for  $\rho$ , we obtain

$$\rho = \frac{1}{C_2} \left[ \ln\left(\frac{E_{0m}}{E_m}\right) + n \cdot \ln(1 - p) \right] \quad (9)$$

Note that the assumption of  $n = 2$  is reasonable, as nanopores can well be approximated as spherical. If we then assume that the dependence of  $\rho$  on  $N$  is an Avrami function

$$\rho = \rho_0 + \rho_1 \cdot \left[ 1 - \exp\left(-\frac{N}{N_1}\right) \right] \quad (10)$$

we can extract the fitting parameters:  $\rho_0$  = initial microcrack density;  $\rho_1$  = total microcrack density increment due to cyclic load; and  $N_1$  = characteristic number of cycles (to reach an increment of  $1/e$  of the initial value). The plot is shown in Figure 13, left, and the fitting parameters are shown in Table 4. We remark that while the choice of such fitting function is arbitrary, a kinetic function seems to be appropriate to describe (damage) accumulation. The treatment yields a typical number of cycles to "saturate" damage evolution. It is also to be noted that Gao et al.,<sup>[32]</sup> as well as Bruno et al.,<sup>[33]</sup> have already observed that damage evolution stops after some (few) cycles in porous and microcracked ceramics, and their behavior becomes brittle linear elastic.

From this analysis, we extract an estimation of the increase in microcrack density with respect to the initial one and observe that the matrix is heavily microcracked from the very beginning.

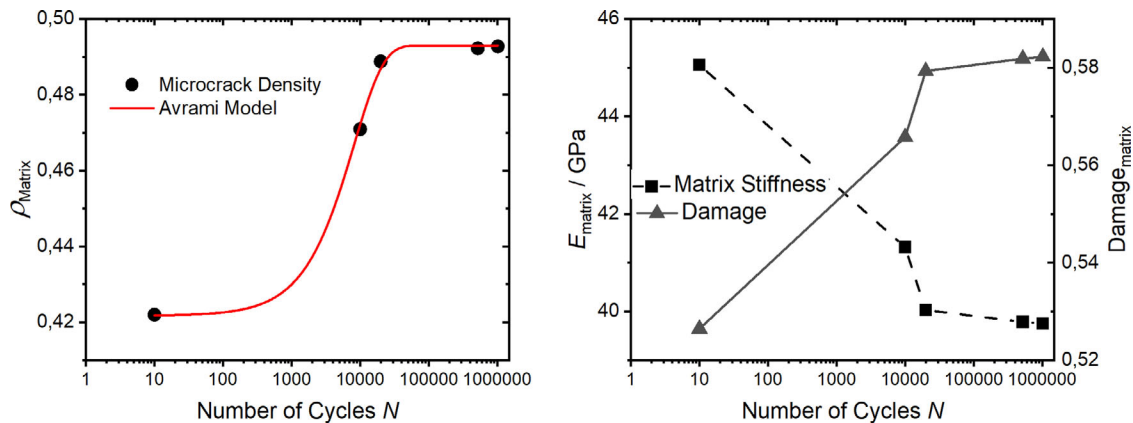


**Figure 13.** Microcrack density parameter, damage parameter, and Young’s modulus as a function of load cycles. For the microcrack density, the fit with an Avrami function is also shown (see text); for the damage parameter (see below) and the matrix stiffness, connecting lines are displayed. Note that data at 0 cycles are artificially shifted to ten cycles for the sake of the logarithmic scale.

**Table 4.** Fitted microcrack parameters (see Figure 13) according to Equation (10).

Fitting Parameter	Value
$\rho_0$	$0.422 \pm 0.002$
$\rho_1$	$0.071 \pm 0.002$
$N_1$	$8200 \pm 600$

Indeed, the material suffers extensive microcracking due to the thermal expansion mismatch between the two constituents (this is analogous to many other ceramic composites such as stabilized aluminum titanate and  $\beta$ -eucryptite, see the study by Bruno et al.<sup>[34]</sup>). The additional microcrack density due to cycling is less than 20%. We also see that in spite of the fact that in the refraction maps no difference can be seen until the specimen is loaded for 520 000 cycles, the increase in microcrack density “saturates” already after 20 000 cycles (in fact, with a decay factor of about 8,000 cycles), as also visible from the behavior of the matrix stiffness; see Figure 13-right.

As an alternative description, one can use the so-called damage parameter  $d$ ,<sup>[5,35]</sup> which for the matrix is defined as

$$d = 1 - \frac{E_m}{E_{0m}} \quad (11)$$

Also in the case of the damage parameter, after an initial strong increase in damage a plateau is reached (Figure 13, right). This behavior is similar to that of the microcrack density parameter (Figure 13). This is due to the fact that, as shown by Kachanov<sup>[36]</sup> and Mazars,<sup>[37]</sup> the damage and the microcrack density parameters are equivalent concepts for small amounts of microcracking (or, as in our case, microcrack density increments). In fact, one can write the term  $\exp(-C_2\rho)$  in Equation (8) as a first-order Taylor expansion in the form  $(1 - C_2 \cdot \rho)$ ; by comparison with the definition of  $d$  (Equation (11)), one would come to the conclusion that  $d \sim C_2\rho$ . It must be noted that for large amounts of damage

(microcracking) this equivalence is only approximate: in our case, the initial microcracking is so large that the damage approach only fully agrees with the more rigorous Kachanov theory because we start from a very large damage parameter and calculate its increment. In other words, it is recommended to use a more rigorous micromechanics rather than the damage mechanics approach, to avoid unnecessary approximations.

A final comment is also due: we have calculated the microcrack density (and the damage parameter) assuming microcracking being confined to the matrix. If we would evaluate them using, instead of Equation (8) or (11), the following

$$\begin{cases} \frac{E_c}{E_{0c}} = (1 - p_{\text{total}})^n \cdot \exp(-C_2\rho_{\text{total}}) \\ d_{\text{total}} = 1 - \frac{E_c}{E_{0c}} \end{cases} \quad (12)$$

with  $E_{0c}$  = Young’s modulus of the dense composite (matrix + fibers), calculated with a crude rule of mixtures, and  $\rho_{\text{total}}$  and  $d_{\text{total}}$  = composite microcrack density and damage parameter, respectively, we would get the same results as shown in Figure 13 and in Table 4 up to 1% difference. This confirms that damage is indeed confined in the matrix.

## 5. Conclusion

We showed that an alumina–zirconia matrix laminate composite with Nextel 610 fiber reinforcement undergoes damage accumulation upon cyclic tensile loading. We observed that the stiffness of the composite decreases with the number of cycles relatively quickly (the first 20 000 cycles are enough to reach damage or microcracking saturation). Using an original modeling strategy and two similar but independent modeling approaches (damage mechanics and the micromechanical differential scheme), we were able to quantify the amount of microcracking occurring as a function of number of cycles and estimate the initial microcrack density (due to the thermal expansion mismatch between the two matrix constituents). In modeling, the porosity was assigned only to the matrix, as the fibers consist of dense alumina. In addition, it was assumed that microcrack formation

is limited to the porous matrix, because it has a significantly lower strength compared with the fibers and is prone to cracking even at very low stresses. The assumptions were later verified. Through the synergistic use of SXRR, SEM, and mechanical properties, we could arbitrate on the acting damage mechanisms: as the internal specific surface of defects (proportional to the X-ray refraction intensity) actually decreases for large numbers of cycles (but also the Young's modulus decreases, i.e., the amount of microcracking increases), we can deduce that first microcrack propagation is dominant over microcrack nucleation (which would increase the internal specific surface), but then nucleation also takes place, though to a minor extent. This is somewhat different to what we found in other microcracked ceramics such as  $\beta$ -eucryptite, aluminum titanate, and cordierite.

## Acknowledgements

The authors thank colleagues from HZB, Berlin, Germany, for their support as well as Ralf Britzke and Thomas Wolk (BAM) for their assistance during beam time at the BAMline.

Open access funding enabled and organized by Projekt DEAL.

## Conflict of Interest

The authors declare no conflict of interest.

## Data Availability Statement

The data that support the findings of this study are available from the corresponding author upon reasonable request.

## Keywords

ceramic matrix composites, homogenization schemes, microcracking, nonlinear behaviors, synchrotron X-ray refraction radiography

Received: June 18, 2021

Revised: August 18, 2021

Published online:

- [1] a) A. G. Evans, *J. Am. Ceram. Soc.* **1990**, *73*, 187; b) R. Warren, *Ceramic-Matrix Composites*, Blackie Academic and Professional, Glasgow, London **1992**; c) K. K. Chawla, *Ceramic Matrix Composites* Chapman & Hall, London, UK **1993**, p. 212, DOI: [https://doi.org/10.1007/978-1-4757-2966-5\\_7](https://doi.org/10.1007/978-1-4757-2966-5_7).
- [2] a) P. E. D. Morgan, D. B. Marshall, *Mater. Sci. Eng. A* **1993**, *162*, 15; b) A. G. Evans, M. Y. He, J. W. Hutchinson, *J. Am. Ceram. Soc.* **1989**, *72*, 2300; c) A. Evans, F. Zok, J. Davis, *Compos. Sci. Technol.* **1991**, *42*, 3; d) A. G. Evans, F. W. Zok, *J. Mater. Sci.* **1994**, *29*, 3857.
- [3] a) M. Y. He, J. W. Hutchinson, *J. Appl. Mech.* **1989**, *56*, 270; b) M. Y. He, J. W. Hutchinson, *Int. J. Solids Struct.* **1989**, *25*, 1053.
- [4] a) R. J. Kerans, R. S. Hay, T. A. Parthasarathy, M. K. Cinibulk, *J. Am. Ceram. Soc.* **2002**, *85*, 2599; b) K. T. Faber, *Annu. Rev. Mater. Sci.* **1997**, *27*, 499; c) R. J. Kerans, T. A. Parthasarathy, *Composites Part A* **1999**, *30*, 521.
- [5] J. Lemaître, in *A Course on Damage Mechanics*, Springer Verlag, **1996**, 5.
- [6] a) J. F. Maire, P. M. Lesne, *Aerospace Sci. Technol.* **1997**, *1*, 259; b) J. L. Chaboche, J. F. Maire, *Aerospace Sci. Technol.* **2002**, *6*, 131; c) J. L. Chaboche, J. F. Maire, *Compos. Sci. Technol.* **2001**, *61*, 2239; d) G. Camus, *Int. J. Solids Struct.* **2000**, *37*, 919; e) J. Xie, G. Fang, Z. Chen, J. Liang, *Compos. Struct.* **2017**, *176*, 164; f) K. Tushtev, J. Horvath, D. Koch, G. Grathwohl, *Adv. Eng. Mater.* **2004**, *6*, 664.
- [7] a) W. C. Tu, F. F. Lange, A. G. Evans, *J. Am. Ceram. Soc.* **1996**, *79*, 417; b) T. J. Lu, *J. Am. Ceram. Soc.* **1996**, *79*, 266; c) F. F. Lange, W. C. Tu, A. G. Evans, *Mater. Sci. Eng. A* **1995**, *195*, 145; d) C. G. Levi, J. Y. Yang, B. J. Dalgleish, F. W. Zok, A. G. Evans, *J. Am. Ceram. Soc.* **1998**, *81*, 2077.
- [8] a) E. Volkman, A. Dentel, K. Tushtev, C. Wilhelmi, K. Rezwani, *J. Mater. Sci.* **2014**, *49*, 7890; b) R. S. M. Almeida, Y. Li, B. Besser, P. Xiao, W. Zhou, A. Brückner, N. Langhof, K. Tushtev, W. Krenkel, K. Rezwani, *J. Eur. Ceram. Soc.* **2019**, *39*, 2244.
- [9] a) N. Godin, P. Reynaud, G. Fantozzi, *Eng. Frac. Mech.* **2019**, 210452; b) N. Guel, Z. Hamam, N. Godin, P. Reynaud, O. Caty, F. Bouillon, A. Paillassa, *Materials* **2020**, *13*, 4691; c) G. Morscher, Z. Han, *Materials* **2018**, *11*, 2477; d) C. B. Ramdane, A. Julian-Jankowiak, R. Valle, Y. Renollet, M. Parlier, E. Martin, P. Diss, *J. Eur. Ceram. Soc.* **2017**, *37*, 2919.
- [10] a) J. Thornton, B. D. Arhatari, M. Sesso, C. Wood, M. Zonneveldt, S. Y. Kim, J. A. Kimpton, C. Hall, *Microsc. Microanal.* **2019**, *25*, 583; b) A. M. Hilmas, G. Henson, A. Singhal, Y. Gao, M. Schuster, *Ceram. Int.* **2020**, *46*, 13502; c) L. Saucedo-Mora, T. Lowe, S. Zhao, P. D. Lee, P. M. Mummery, T. J. Marrow, *J. Nucl. Mater.* **2016**, *481*, 13.
- [11] A. Kupsch, B. R. Müller, A. Lange, G. Bruno, *J. Eur. Ceram. Soc.* **2017**, *37*, 1879.
- [12] M. P. Hentschel, R. Hosemann, A. Lange, B. Uther, R. Bruckner, *Acta Crystallograph. A* **1987**, *43*, 506.
- [13] a) M. Erdmann, A. Kupsch, B. R. Müller, M. P. Hentschel, U. Niebergall, M. Böhning, G. Bruno, *Journal of Materials Science*, **2019**, *54*, 11739; b) D. Schob, R. Roszak, I. Sagradov, H. Sparr, M. Ziegenhorn, A. Kupsch, F. Léonard, B. R. Müller, G. Bruno, *Archives of Mechanics*, **2019**, *71*, 507; c) D. Schob, I. Sagradov, R. Roszak, H. Sparr, R. Franke, M. Ziegenhorn, A. Kupsch, F. Léonard, B. R. Müller, G. Bruno, *Eng. Fract. Mech.* **2020**, *229*, 106841.
- [14] B. R. Müller, M. P. Hentschel, in *Handbook Of Technical Diagnostics - Fundamentals And Application To Structures And Systems*, (Ed: H. Czichos), Springer, New York **2013**, p. 287.
- [15] a) B. R. Müller, R. C. Cooper, A. Lange, A. Kupsch, M. Wheeler, M. P. Hentschel, A. Staude, A. Pandey, A. Shyam, G. Bruno, *Acta Mater.* **2018**, *144*, 627; b) R. Laquai, F. Gouraud, B. R. Müller, M. Huger, T. Chotard, G. Antou, G. Bruno, *Materials* **2019**, *12*, 1017; c) D. E. Mack, R. Laquai, B. R. Müller, O. Helle, D. Sebold, R. Vaßen, G. Bruno, *J. Am. Ceram. Soc.* **2019**, *102*, 6163, DOI: <https://doi.org/10.1111/jace.164651>.
- [16] S. Evsevlev, B. R. Müller, A. Lange, A. Kupsch, *Nucl. Instrum. Methods Phys. Res. A* **2019**, *916*, 275.
- [17] R. C. Cooper, G. Bruno, M. R. Wheeler, A. Pandey, T. R. Watkins, A. Shyam, *Acta Mater.* **2017**, *135*, 361.
- [18] W. E. C. P. Spezialkeramik, W.E.C. Pritzkow Spezialkeramik, **2012**, [https://www.keramiklech.com/fileadmin/user\\_upload/pdf/New\\_materials.pdf](https://www.keramiklech.com/fileadmin/user_upload/pdf/New_materials.pdf) (accessed: March 2021).
- [19] a) B. R. Müller, A. Lange, M. Harwardt, M. P. Hentschel, *Adv. Eng. Mater.* **2009**, *11*, 435; b) W. Görner, M. P. Hentschel, B. R. Müller, H. Riesemeier, M. Krumrey, G. Ulm, W. Diete, U. Klein, R. Frahm, *Nucl. Instrum. Meth. Phys. Res. A* **2001**, *467*, 703.
- [20] a) A. Lange, M. P. Hentschel, A. Kupsch, B. R. Müller, *Int. J. Mater. Res.* **2012**, *103*, 174; b) A. A. M. Al-Falahat, A. Kupsch,

- M. P. Hentschel, A. Lange, N. Kardjilov, H. Markötter, I. Manke, *Rev. Sci. Instrum.* **2019**, *90*, 125108.
- [21] C. A. Schneider, W. S. Rasband, K. W. Eliceiri, *Nat. Methods* **2012**, *9*, 671.
- [22] a) J. Nellesen, R. Laquai, B. R. Müller, A. Kupsch, M. P. Hentschel, N. B. Anar, E. Soppa, W. Tillmann, G. Bruno, *J. Mater. Sci.* **2018**, *53*, 6021; b) S. Cabeza, B. R. Müller, R. Pereyra, R. Fernandez, G. Gonzalez-Doncel, G. Bruno, *J. Appl. Crystallograph.* **2018**, *51*, 420, <https://doi.org/10.1107/S1600576718001449>.
- [23] R. Laquai, B.R. Müller, G. Kasperovich, G. Requena, J. Haubrich, G. Bruno, *Mater. Perform. Char.* **2020**, *9* 82.
- [24] a) G. Bruno, M. Kachanov, *J. Am. Ceram. Soc.* **2016**, *99* 3829; b) G. Bruno, M. Kachanov, *J. Eur. Ceram. Soc.* **2013**, *33* 2073; c) M. Kachanov, I. Sevostianov, in *Micromechanics of Materials, with Applications*. Springer, Heidelberg, Berlin **2018**, p. 649.
- [25] R. Hill, *J. Mech. Phys. Solids* **1963**, *11*, 357.
- [26] A. Reuss, *Z. Angew. Math. Mech* **1929**, *9*, 49.
- [27] W. Voigt, *Wied. Ann.* **1889**, *38*, 573.
- [28] G. Bruno, M. Kachanov, I. Sevostianov, A. Shyam, *Acta Mater.* **2019**, *164*, 50.
- [29] <https://multimedia.3m.com/mws/media/1327055O/3m-nextel-technical-reference-guide.pdf> (accessed Jan 2021).
- [30] G. Bruno, A. M. Efremov, C. P. An, B. R. Wheaton, D. J. Hughes, *J. Mater. Sci.* **2012**, *47*, 3674.
- [31] L. Gibson, M. Ashby, *Proc. Roy. Soc. London* **1982**, *A382*, 43.
- [32] Z. Gao, J. W. Zimmerman, M. Kachanov, *Int. J. Fract.* **2013**, *183*, 283.
- [33] G. Bruno, M. Kachanov, I. Sevostianov, A. Shyam, *Acta Mater.* **2019**, *164*, 50.
- [34] a) G. Bruno, O. V. Garlea, J. Muth, A. M. Efremov, T. R. Watkins, A. Shyam, *Acta Mater.* **2012**, *60*, 4982; b) G. Bruno, A. M. Efremov, B. R. Wheaton, I. Bobrikov, V. G. Simkin, S. Mixture, *J. Eur. Ceram. Soc.* **2010**, *30*, 2555; c) A. M. Efremov, G. Bruno, *Phil. Mag.* **2013**, *93* 691.
- [35] D. Krajcinovic, *Mech. Mater.* **1989**, *8*, 117.
- [36] M. L. Kachanov, *Mech. Mater.* **1982**, *1*, 19.
- [37] G. Pijaudier-Cabot, J. Mazars, in J. Lemaitre (ed.), *Handbook of Materials Behavior*, Vol. II, Academic Press, San Diego **2001**, p. 500.